

Sustainable Soy Protein Microsponges for Efficient Removal of Lead (II) from aqueous environments

Sara Anselmo ^{a,†}, Tiziana Avola ^{b,†}, Kleopatra Kalouta ^{c,d}, Salvatore Cataldo ^a, Giuseppe Sancataldo ^a, Nicola Muratore ^a, Vito Foderà ^c, Valeria Vetri ^{a*}, Alberto Pettignano ^{a*}

^a Dipartimento di Fisica e Chimica – Emilio Segrè, Università di Palermo, Viale delle Scienze, I-90128 Palermo, Italy

^b Dipartimento di Chimica, Università di Milano, via Golgi 19, I-20133 Milano, Italy

^c Dipartimento di Scienze e Tecnologie Biologiche Chimiche e Farmaceutiche (SteBiCeF), Università di Palermo, Viale delle Scienze, I-90128 Palermo, Italy

^d Department of Pharmacy, University of Copenhagen, Universitetsparken 2, 2100 Copenhagen, Denmark

[†] These authors contributed equally

* Corresponding authors:

alberto.pettignano@unipa.it, valeria.vetri@unipa.it

Abstract

Biomaterials capable to efficiently remove heavy metals, hazardous to the human health and ecosystem, from water are nowadays of great interest in many research fields. The design and fabrication of these materials should be based on a sustainable processing and rely on the biocompatibility of the building blocks which can derive from renewable sources. Protein-based materials emerge as good candidates for water cleaning applications, due to the large availability of the constituent material, their biocompatibility and the ease of preparation. In this work, aggregates of Soy Protein Isolate (SPI) were produced in aqueous solution at different pHs to obtain micron-sized sponge-like structures with adsorbent properties. By suitably varying solution conditions, we tuned the molecular structure of these protein aggregates and, in turn, their physicochemical properties, namely hydrophobicity and water accessibility. Their efficiency in removing lead (Pb^{2+}) ions from aqueous solutions was evaluated by investigating the adsorption mechanisms and thus providing new insights on the relation between structural features of the self-assembled material and the capability of binding the metal.

Keywords - Lead, soy, amyloid superstructures, adsorption, green chemistry, water contamination

1. INTRODUCTION

Contamination of aquatic systems is a serious environmental issue causing diseases and death for people, plants and living organisms worldwide. A principal source of water pollution is the industry,

36 which releases increasing amounts of toxic pollutants in the environment, including heavy metals.
37 The latter are eco-toxicological hazards, they do not degrade and they accumulate in vital organs of
38 humans and animals causing irreversible damages¹⁻³.
39 In order to improve environmental sustainability, rational and efficient wastewater management is
40 needed and water must be purified at the level of being safe for drinking, washing, and for being
41 released into rivers, lakes and the sea⁴. Currently, various technologies exist for water purification
42 such as sorption⁵, chemical precipitation⁶, ion exchange⁷, reverse osmosis⁸ and electrochemical
43 treatment⁹. Among those, sorption emerges as a promising solution due to its high efficiency, low-
44 cost, and ease of operation¹⁰⁻¹²; for these reasons, research is ongoing for new biocompatible sorbent
45 materials.
46 Several kinds of natural sorbent materials such as fungi¹³, algae¹⁴, bacteria^{15,16} and by-products from
47 industrial processes¹⁷ are currently under the lens of scientists for their potential low environmental
48 impact. Moreover, polymeric adsorbents, which have shown a high removal capability of heavy metal
49 ions from wastewater¹⁸, have been tested. Biopolymers, such as cellulose, calcium alginate, pectate,
50 polygalacturonate and starch have shown interesting properties as adsorbents for water treatment due
51 to their biodegradability¹⁹⁻²¹. In this context, proteins are emerging as promising eco-compatible
52 binding blocks for the production of new green absorbers, containing functional groups with metal-
53 binding capability^{10,22,23}. Side chains of cysteine, aspartic acid, glutamic acid, and histidine are the
54 most favored motifs to coordinate heavy metals²⁴.
55 The possibility to induce supramolecular association of protein molecules and to tailor the structural
56 properties of newly formed bidimensional or tridimensional structures, at molecular level, paves the
57 way for the design of tailored materials for different applications²⁵. A plethora of structures such as
58 fibrils, spherical condensates and gels, can be generated with sizes ranging from the nano to the
59 macroscopic scale. The structures of these bidimensional or tridimensional supramolecular
60 assemblies as well as their mechanical properties, charge, polarity, water accessibility, and the
61 stability of these materials can be tuned by regulating the growth conditions²⁶⁻²⁹. In particular,
62 amyloid fibrils have shown good capability to remove heavy metals and other water pollutants from
63 water, this property being also attributed to the presence of a high content of intermolecular β -
64 structures, which are considered to be an essential feature for water purification properties^{23,30-32}.
65 In a previous work²², we have demonstrated the excellent Pb^{2+} ions adsorption efficiency of Bovine
66 Serum Albumin (BSA) micro-sized amyloid-like spherical particles. A complex adsorption
67 mechanism was highlighted, resulting from the balance between specific interactions with functional
68 groups in protein structure and heterogeneous interactions common to polypeptide chains. These

features were related to the amyloid state and modifications of the hydration layer of protein microparticles²².

In the present work, we generate a material based on a renewable building block, Soy Protein Isolate (SPI), by using green chemistry principles. SPI is a plant-based extract from the soybean oil production industry, which emerges as a good candidate for new functional, multipurpose materials, being green, intrinsically biocompatible, biodegradable, abundant in nature and cost-effective^{33–35}.

The trimer, glycoprotein β -conglycinin (7S) and the hexamer glycinin (11S) are the two major protein fractions in SPI³⁶ the isoelectric point of which is reported to be in the pH 4–5 interval³⁷.

Soy protein in combination with polymers was previously used to create hybrid materials for water purification³⁸, including microspheres or hydrogels^{10,39}.

Here, we show the possibility of obtaining SPI microsponges with amyloid-like molecular structures by simply incubating SPI aqueous solutions at high temperature and at two different pHs, namely pH 5 and pH 9, which are close and away from the isoelectric point of SPI, respectively. This in the light of the idea that, in addition to the binding sites intrinsically present in proteins such as hydroxyl, amino, and other active functional groups²⁴, the three-dimensional structure of microsponges could benefit from porosity (which makes them solvent-accessible), large surface area and open-hole structure for metal adsorption.

The rationale of this study lies on the well supported hypothesis that by modulating solution conditions it is possible to control the structure and physicochemical properties of protein aggregates^{26–28,40}. The SPI protein microstructures are significantly different at molecular level and in terms of physicochemical properties, i.e. polarity and water accessibility, translating in a highly different metal binding affinity.

The efficiency of these microsponges in removing the Pb^{2+} ion from aqueous solutions was evaluated by Differential Pulse Anodic Stripping Voltammetry (DP-ASV) technique. The experimental data of adsorption kinetics were processed with the pseudo first order, pseudo second order and pseudo n order kinetic equations, whilst Langmuir and Freundlich equations were used to process the data of isotherm adsorption. The complex adsorption mechanisms and different efficiency were explained in relation to the structural properties of the microsponges, highlighting the role of the different polarity of the internal cavities.

2. MATERIALS AND METHODS

2.1 Reagents

Vitablend Unisol DP IP Non GMO soy protein isolate (SPI, >90% protein) was kindly provided by Barentz ApS (Hoodorp, HB, The Netherlands). Thioflavin T $\geq 65\%$, Nile Red $\geq 98\%$, potassium phosphate monobasic $\geq 99\%$, potassium phosphate dibasic $\geq 99\%$ were purchased from Sigma-Aldrich. Sodium nitrate and sodium chloride pure salts (Fluka) were used, after drying at 383.15 K for 2 h. Nitric and hydrochloric acids and sodium hydroxide used to adjust the pH of the Pb^{2+} ion solutions were prepared by diluting concentrated Fluka solutions. Pb^{2+} ion solutions were prepared by weighing the $\text{Pb}(\text{NO}_3)_2$ (Aldrich, analytical grade) salt. Pb^{2+} standard solutions used for calibration curve were prepared by diluting a 1000 mg L^{-1} standard solution in 2% HNO_3 (CertiPUR, Merck). All the solutions were prepared using freshly, CO_2 -free ultra-pure water ($\rho \geq 18 \text{ M}\Omega \text{ cm}$) and grade A glassware.

2.2 Samples preparation

The samples were formed by dispersing 1.5 mg mL^{-1} of soy protein in 0.1 mol L^{-1} K-phosphate buffer at pH 5 and pH 9 and incubating at 323.15 K for 24 h, using 50 mL falcon tubes, immersed in a water bath. The samples were spun down by centrifugation (7500 rpm, 10 minutes) and washed with ultra-pure water ($\sim 25 \text{ mL}$), to remove the buffer solution, and then freeze dried (0.2 mbar, 233.15 K). From now on, these samples will be indicated as Soy-5 and Soy-9.

2.3 Samples characterization

2.3.1 Fourier Transform Infrared microscopy (micro-FTIR) measurements

Micro-FTIR measurements were performed at room temperature using a LUMOS Fourier Transform Infrared microscope (Bruker) equipped with a photoconductive MCT detector with liquid nitrogen cooling. Visual image collection was performed via a fast digital CCD camera, integrated in the instrument. Samples dispersed in D_2O at a final concentration of 20 mg mL^{-1} , were placed between two CaF_2 windows, separated by a 50 μm Teflon spacer. FTIR spectra were collected in the range 4000-400 cm^{-1} . Each final spectrum was the average of 128 scans. The variable microscope aperture was set to squared regions of interest (ROIs) with a 25 μm x 25 μm size.

Fitting of the Amide I' band was performed in terms of five Gaussian components. The Gaussian function (Eq. 1) was used:

$$I(\nu) = \sum_{i=1}^n A_i e^{-\frac{(\nu-\nu_i)^2}{2\sigma_i^2}} \quad (\text{Eq. 1})$$

, where I is the intensity and ν_i , σ_i and $A_i = \frac{1}{\sigma_i \sqrt{2\pi}}$ are the frequency, the width and the area of the i^{th} component, respectively. During the fitting procedure, the peak frequency of the selected five components was kept fixed at 1610 cm^{-1} , 1620 cm^{-1} , 1640 cm^{-1} , 1660 cm^{-1} and 1676 cm^{-1} and the

spectral width was shared. The fractional area, indicating the relative amount of secondary protein structure in each spectrum, was defined by the following equation (Eq. 2):

$$A_i (\%) = \frac{A_i}{\sum_{i=1}^n A_i} \% \quad (\text{Eq. 2})$$

2.3.2 Confocal and Fluorescence Lifetime Imaging microscopy (FLIM)

Samples with a final protein concentration of 20 mg mL⁻¹ were stained with 40 μmol L⁻¹ Thioflavin T (ThT) and 60 μmol L⁻¹ Nile Red. 250 μL of samples were placed in microscope chambered slides and imaged at 1024x1024 pixel resolution, using a Leica TCS SP5 confocal laser scanning microscope and a 63x objective (Leica Microsystems, Germany). ThT was excited using λ_{ex} = 470 nm (Leica “white light laser”) and the emission signal was collected in the range 485-630 nm. Nile Red was excited using λ_{ex} = 540 nm and the emission signal was collected in the range 580-700 nm. Fluorescence lifetime imaging measurements were acquired in the time domain by means of a picoHarp 300 standalone TCSPC module (Picoquant). 256x256 images were obtained at a scanning frequency of 400 Hz, using the aforementioned laser parameters for each dye.

2.3.3 FLIM analysis

The phasor analysis, described by Digman et al.⁴¹ was used for FLIM data. Phasor approach is a Fourier domain technique that allows the transformation of the signal in every pixel of the image to a single point called “phasor” in the phasor plot. In this representation, all possible single exponential decays lie on the “universal circle” defined as a semicircle, with radius 1/2, going from point (0, 0), corresponding to τ = ∞, to point (1, 0), corresponding to τ = 0. On the contrary, complex decays are represented by phasors within the universal circle. Importantly, given that the phasors follow the vector algebra, it is possible to geometrically resolve the fractions of two fluorescent species (in the simplest case) by the lever rule of vector additions. Indeed, the linear combination of two single-exponential decay components generates phasors within the universal circle, which lie on a straight line joining the phasors of the two single components. The contribution/fraction from one single component to the lifetime is proportional to its distance from the phasor. In the phasor plot, it is also possible to select these lifetime distributions using colored cursors and the corresponding pixels will result with the same color of the cursors to the image pixels by which the so-called “lifetime maps” are obtained. FLIM data have been processed by the SimFCS software (Laboratory for Fluorescence Dynamics, University of California, Irvine, CA, available at www.lfd.uci.edu). FLIM calibration of the system for ThT was performed by measuring the known lifetime of fluorescein that is a single-

172 exponential of 4.0 ns⁴². For Nile Red, lifetime calibration was performed using Alexa594 that has a
173 single-exponential lifetime of 3.9 ns⁴³.

174

175 2.3.4 Attenuated Total Reflectance Fourier Transform Infrared spectroscopy (ATR-FTIR)

176 ATR analysis on Soy-5 and Soy-9 samples, before and after Pb²⁺ adsorption, was conducted using a
177 Bruker ALPHA FTIR spectrometer, equipped with a platinum ATR device. Spectra were recorded in
178 the wavelength range 4000-400 cm⁻¹, as an average of 64 scans and with a spectral resolution of 4
179 cm⁻¹. Background contribution was subtracted from all spectra.

180

181 2.4 Procedures for kinetic, thermodynamic and reuse experiments

182 The kinetic experiments of Pb²⁺ adsorption onto Soy-5 and Soy-9 samples were carried out in a
183 voltammetric cell adding a known amount of the adsorbent material (10-20 mg) to the Pb²⁺ ions
184 solution ($c_{Pb^{2+}} \approx 30 \text{ mg L}^{-1}$, 20 mL) at pH = 5, at $I = 0.10 \text{ mol L}^{-1}$, in NaNO₃ and, only for Soy-9
185 sample, in NaCl, at $T = 298.15 \text{ K}$. The suspension was constantly and regularly stirred and the metal
186 ion concentration, always in excess in respect to Soy-5 and Soy-9 samples, was measured through
187 differential pulse anodic stripping voltammetry (DP-ASV) measurements at various
188 adsorbent/solution contact times in the interval 0 - 400 minutes. The voltammetric apparatus,
189 controlled by NOVA v. 1.10 software, was constituted by a Metrohm 663 VA stand combined with
190 the Autolab potentiostat in conjunction with the IME663 interface. The VA stand was equipped with
191 a three-electrode system consisting of: *i*) a MultiMode Electrode Pro (Metrohm, code 6.1246.120)
192 working in the Static Mercury Drop Electrode (SMDE) mode; *ii*) a glassy carbon auxiliary electrode
193 (code 6.1247.000); *iii*) a double junction Ag/AgCl/ KCl (3 mol·L⁻¹) reference electrode (code
194 6.0728.030). The DP-ASV measurements were performed after bubbling purified N₂ gas into the
195 solutions for 150 s. The experimental electrochemical conditions were chosen in order to optimize
196 the quality parameters, as signal/noise ratio, repeatability and accuracy (deposition potential -0.55 V;
197 deposition time 1 s; equilibration time 10 s; potential interval -0.55 to -0.20 V; scan rate 0.01 V s⁻¹;
198 step potential 3 mV; modulation amplitude 50 mV; modulation time 0.01 s; interval time 0.2 s). The
199 voltammetric apparatus was calibrated at the same experimental conditions of the adsorption kinetic
200 experiments.

201 Isotherm experiments were carried out for Soy-5 and Soy-9 samples at initial pH = 5.00, in NaNO₃
202 0.10 mol L⁻¹ and $T = 298.15 \text{ K}$. Only for Soy-9 sample, the isotherm adsorption experiments were
203 extended in the pH range 4.00 - 6.50, at $I \rightarrow 0 \text{ mol L}^{-1}$ and in the ionic strength range $0.05 \leq I (\text{mol L}^{-1}) \leq 0.5$, in the ionic media NaCl and NaNO₃. All isotherm experiments were carried out in batch, at
204 room temperature ($T = 293.15 \text{ K}$), placing different amounts (5-20 mg) of the protein samples

investigated in different Erlenmeyer flasks containing 20 - 40 mL of a $\text{Pb}(\text{NO}_3)_2$ solution ($c_{\text{Pb}^{2+}} \approx 30$ mg L^{-1}) at the established experimental conditions. The suspensions were stirred at 180 rpm for 24 h using an orbital mixer (model M201-OR, MPM Instruments) and then were separated from the adsorbent material before measuring the pH and the metal ion concentration.

The reuse and recycling of Soy-5 and Soy-9 samples were studied by packing ~ 5 mg of the adsorbent into a glass column (diameter = 2 cm, length = 10 cm). A volume of 15 mL of $\text{Pb}(\text{NO}_3)_2$ solution ($c_{\text{Pb}^{2+}} \approx 30$ mg L^{-1} , pH = 5, $T = 298.15$ K) was flowed at reflux into the column with a flow rate of 6 mL min^{-1} for 16 h (the reaching of adsorption equilibrium was verified) by using a peristaltic pump (Gilson, Minipuls 3). The sorbent material was then washed with 100 mL of distilled water before the reflux with 15 mL of EDTA 0.1 mol L^{-1} solution for 7 h. After a further washing with 100 mL of distilled water, the next adsorption/desorption cycle began. The solutions derived from each adsorption/desorption step were collected in test tubes. Four adsorption/desorption cycles were carried out. The metal ion concentrations in the solutions collected in isotherm and in the adsorption steps of reuse experiments were measured by the same voltammetric apparatus previously used in kinetic experiments. Due to the presence of EDTA, some experimental electrochemical conditions of the voltammetric cell were modified to measure the lead concentrations in solutions derived from desorption steps (deposition potential -1.15 V; deposition time 90 s; potential interval -1.15 to -0.20 V). The voltammetric cell was previously calibrated at the same experimental conditions of the analysed solutions.

The pH of the solutions collected during the adsorption experiments was measured with a combined ISE- H^+ glass electrode (Ross type 8102) previously calibrated at the same experimental conditions.

2.5 Kinetic and isotherm models for Pb^{2+} adsorption onto Soy-5 and Soy-9 samples

The kinetic data of Pb^{2+} ions adsorption onto the Soy-5 and Soy-9 samples were tentatively fitted with three kinetic models: i) the most used pseudo-first order (PFO)⁴⁴ (Eq.3) and ii) pseudo-second order (PSO)⁴⁵ (Eq.4) equations and iii) the pseudo n order equation (PGO)⁴⁶ (Eq.5). The relevant integrating non-linear equations for the boundary conditions $t = 0$ to $t = t$ and $q_t = 0$ and $q_t = q_t$ used in data processing are listed below (Eq. 3 – 5):

$$q_t = q_e (1 - e^{-k_1 t}) \quad (\text{Eq. 3})$$

$$q_t = \frac{q_e^2 k_2 t}{1 + q_e k_2 t} \quad (\text{Eq. 4})$$

$$q_t = q_e - \frac{q_e}{(k_n q_e^{(n-1)} t^{(n-1)+1})^{\frac{1}{(n-1)}}} \quad \text{with } n \neq 1 \quad (\text{Eq. 5})$$

where q_t and q_e are the adsorption capacity of the adsorbent material (mg g^{-1}) at adsorbent/solution contact time t and at the equilibrium, k_1 (min^{-1}), k_2 ($\text{g mg}^{-1} \text{min}^{-1}$) and k_n ($\text{min}^{-1} (\text{g mg}^{-1})^{n-1}$) are the rate constants of the PFO, PSO and PGO models, respectively and n represents the general order of adsorption of the PGO model.

The adsorption equilibria data at different experimental conditions have been processed with the Freundlich⁴⁷ (Eq. 6) and Langmuir⁴⁸ (Eq. 7) isotherm models:

$$q_e = K_F c_e^{1/n} \text{ (Eq. 6)}$$

$$q_e = \frac{q_m K_L c_e}{1 + K_L c_e} \text{ (Eq. 7)}$$

where q_m (mg g^{-1}) is the maximum adsorption capacity of the Soy-5 and Soy-9 samples, c_e (mg L^{-1}) is the Pb^{2+} ions concentration in solution at equilibrium; K_F ($\text{L}^{1/n} \text{g}^{-1} \text{mg}^{1-1/n}$) and K_L (L mg^{-1}) are the Freundlich and Langmuir constants, respectively.

The Pb^{2+} ions adsorption capacity at different contact times (q_t) in kinetic studies or at adsorption equilibrium q_e at different Pb^{2+} /protein aggregate ratios in the isotherm experiments were calculated by the following equation (Eq. 8):

$$q_t \text{ or } q_e = \frac{V(c_0 - c_t)}{m} \text{ (Eq. 8)}$$

where V (L) is the volume of the Pb^{2+} ion solution and m is the mass of Soy-5 and Soy-9 samples (g); c_0 and c_t are the Pb^{2+} ion concentrations in the solutions (mg L^{-1}) at $t = 0$ and $t = t$, respectively. At equilibrium, eq. 6 was used by replacing c_t with c_e to calculate q_e .

The LIANA and OriginLab suite software (OriginLab Corporation, Northampton, Massachusetts, USA) were used to fit kinetic and isotherm equations to experimental data.

3. RESULTS AND DISCUSSION

3.1 Characterization of secondary protein structure by Fourier Transform Infrared microscopy (micro-FTIR)

Soy protein isolate was treated at high temperature in order to obtain protein microstructures with different structural properties. The two different samples were produced by incubating 1.5 mg mL^{-1} of protein solution in phosphate buffer (0.1 mol L^{-1}) pH 5.0 and pH 9.0 at 323.15 K for 24 h. After washing procedures, the samples were freeze dried (see methods for details) to obtain stable powders. From now on, these samples will be indicated as Soy-5 and Soy-9.

In Fig. 1 a) and b) we report the $360 \mu\text{m} \times 280 \mu\text{m}$ optical images of the Soy-5 and Soy-9 samples, respectively, dispersed in D_2O solution at a concentration of 20 mg mL^{-1} . Micron-sized protein

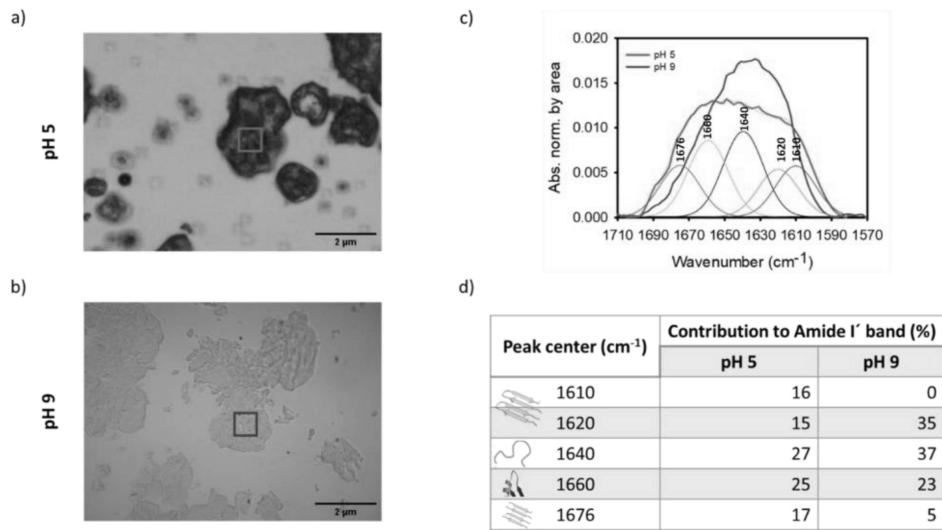
aggregates are present in both samples. Interestingly, the Soy-5 sample has a darker appearance with respect to the Soy-9 sample, which is translucent. This suggests that the microparticles are characterized by different refractive index and that the darker color could be attributed to a more compact structure in the Soy-5 sample⁴⁹. The different optical properties reflected by opacity or transparency of the aggregates can be related to differences in water retention capacity and to different structural features or levels of order⁴⁹.

To verify that, we acquired micro-FTIR absorption spectra at single aggregate level in the 25 μm x 25 μm ROIs, indicated by the colored squares in panel a) and b) of Fig. 1. Spectra in the Amide I' region (1710 cm^{-1} -1570 cm^{-1}) for Soy-5 sample (pink line) and Soy-9 sample (green line) are shown in Fig.1 c). Data are normalized to the band area and the selected Gaussian components used for the deconvolution of these peaks are also shown.

The Amide I' spectral region contains information about protein secondary structure. The detailed analysis of this peak can provide information on the orientation of β -strands forming the intermolecular β -sheets (parallel vs antiparallel), and the strength of inter-strand hydrogen bonds or the number of strands composing the sheet⁵⁰. Soy-9 sample presents a narrower peak, centred at around 1640 cm^{-1} , while the spectrum of Soy-5 sample appears to be significantly broader indicating a larger structural heterogeneity. The Amide I' deconvolution of the bands for the two samples was performed using five Gaussian components, namely 1610 cm^{-1} , 1620 cm^{-1} , 1640 cm^{-1} , 1660 cm^{-1} , 1676 cm^{-1} (Fig. 1c) and results of the fit are reported in Fig. 1 d). This fit is aimed at comparing the two aggregate species, highlighting the presence of native and aggregated structures. The 1610 cm^{-1} and 1620 cm^{-1} peaks are assigned to intermolecular β -sheets^{50,51}, which often represent the fingerprint of amyloid-like structures. The component at 1610 cm^{-1} is aimed at representing the presence of intermolecular β -structure components with stronger H-bonds or longer β -chains^{52,53}. 1640 cm^{-1} component is assigned to random coils and 1660 cm^{-1} to turn and loops. The peak at 1676 cm^{-1} is assigned to antiparallel intermolecular β -sheets.

Both samples present a similar and high content of random coils (peak at 1640 cm^{-1}), turns and loops (peak at 1660 cm^{-1}) in line with what was previously reported for native SPI⁵⁴. From the presented analysis it is possible to note that the total content of intermolecular β -structures is similar between the two samples (48% for Soy-5 sample and 40% for Soy-9 sample). However, the peak at 1620 cm^{-1} , which can be attributed to intermolecular parallel β -sheets typical of amyloids, is dominant for Soy-9 sample, while the representative component used to describe stronger H-bonds (1610 cm^{-1}) is not present. Soy-5 sample presents all the components assigned to intermolecular β -sheets; 1610 cm^{-1} (16 %), 1620 cm^{-1} (15 %) and 1676 cm^{-1} (17 %), with similar contribution.

299 The structural differences between the samples may affect metal affinity, as amyloid β -structures
300 were identified as key aspects to remove toxic heavy metal ions from water^{22,23,30,32,55}.



301
302
303 **Figure 1.** Representative 360 μm x 280 μm optical images for soy samples (a) Soy-5 and (b) Soy-9 sample, in
304 D_2O . The colored 25 μm x 25 μm squares represent the ROIs where FTIR spectra were collected. (c) FTIR
305 spectra in the Amide I' region (1710 cm^{-1} -1570 cm^{-1}) acquired in each ROI of each image, following the same color code. No significant differences, in terms of spectral shape, were observed by varying ROI position or
306 size within the different microscopic aggregates or within the same aggregate. Representative spectral
307 deconvolution of FTIR spectrum for Soy-5 sample in five Gaussian components with spectral components
308 centred at 1610 cm^{-1} , 1620 cm^{-1} , 1640 cm^{-1} , 1660 cm^{-1} and 1676 cm^{-1} . Each component is assigned to a specific
309 protein secondary structure. (d) Fractions of the total area of the Amide I' spectral region for each of the
310 components used for the deconvolution.
311
312

313 **3.2 Quantitative fluorescence microscopy for probing morphological and structural features**

314
315 In order to gain more information on characteristic features of the samples at high spatial resolution,
316 confocal fluorescence microscopy and fluorescence lifetime imaging measurements were performed
317 on ThT stained samples and results are reported in Fig. 2. ThT is the gold standard fluorescence dye
318 used to specifically characterize amyloid structures and its fluorescence lifetime was shown to be
319 sensitive to the details of the intermolecular β -sheets arrangement⁵⁶⁻⁵⁸.

320 In Fig. 2 a) representative 1024x1024 confocal fluorescence microscopy images of Soy- 5 and Soy-
321 9 samples in water, stained with ThT are shown. Both samples present heterogeneous, micron-sized
322 sponge-like structures with different shapes and sizes. The ThT fluorescence intensity signal for each
323 sample reveals the absence of significant differences in the structural organization within submicron
324 scale. However, in the same experimental conditions, a difference in ThT fluorescence intensity is

325 observed between the two samples with the ThT fluorescence intensity of Soy-9 sample being
326 significantly lower. We retrieved the ThT fluorescence intensity in different ROIs in the images of
327 the two samples and the values are reported in the histograms in Fig. 2 b). This difference can be
328 ascribed to different affinity or accessibility of the dye within the aggregates, differences in the
329 rigidity in ThT environment and/or to distinct molecular features of “below resolution” amyloid
330 structures as sensed by this dye.

331 In Fig. 2 c) we report results of FLIM measurements analyzed by means of the phasor approach. It is
332 a simple Fourier Transform domain technique, which allows, without fitting procedures,
333 transformation of the signal in every pixel of the image, to a point in a polar plot corresponding to the
334 measured fluorescence lifetime. All the possible single exponential lifetimes lie on the universal
335 circle, while complex decays are represented by phasors within the circumference. Fig. 2 c)
336 demonstrates the presence of two distinguishable ThT lifetime distributions for the two samples
337 located within the universal circle (the qualitative analysis of the data is reported in Supporting
338 Materials, Fig. SM1). In the phasor representation, a double exponential decay lies on the line
339 connecting two characteristic single exponential phasors on the universal circle, and the distance
340 between each point of the cloud and the single exponential phasor represents the fraction of each
341 component. As previously reported⁵⁹, it is possible to analyze ThT fluorescence decays using a double
342 exponential decay. The fastest component can be attributed to less specific interaction between ThT
343 and its environment due to increased environmental viscosity, while the slower decay is attributed to
344 more specific interaction between ThT and intermolecular β -structures^{59,60}. As shown in Fig. 2 c),
345 this is possible also for the analysis of the present samples and a straight line passes through the
346 characteristic lifetime distributions of the two samples and connects two single exponential lifetimes
347 identified as $\tau_1=0.5$ ns (green circle) and $\tau_2=2.2$ ns (red circle). These lifetime values are compatible
348 with the ones previously described for ThT lifetime decay^{59,60}.

349 Using this model, the decay will be described as:

350
$$I(t) = F_1 e^{-\frac{t}{\tau_1}} + F_2 e^{-\frac{t}{\tau_2}} \quad (\text{Eq. 9})$$

351 where F_1 and F_2 are the fraction of the single exponential decays with τ_1 and τ_2 representing the fast
352 and slow average lifetimes. FLIM images are colored in false colors according to the F_i fraction of
353 the τ_i component. The scale goes from blue (pure fast component at $\tau_1=0.5$ ns) to red (pure slow
354 component at $\tau_2=2.2$ ns). As expected, aggregates in the image present uniform lifetime within the
355 same sample and the fastest decay is dominant in Soy-9 sample ($F_1=0.50$), when compared with Soy-
356 5 sample ($F_1=0.29$), indicating a more tightly packed organization of β -structures in the Soy-5 sample,
357 which is in line with the FTIR measurements.

358

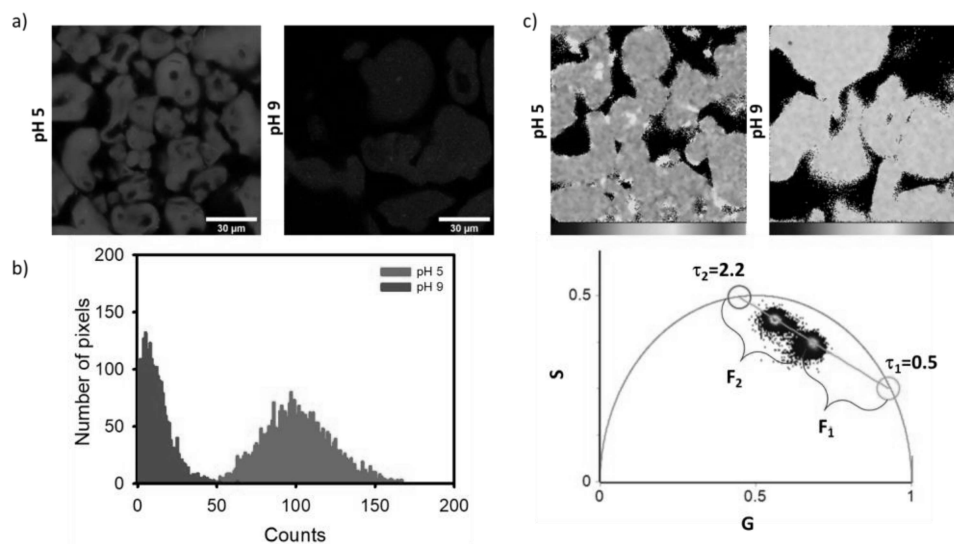


Figure 2. (a) 1024x1024 representative confocal fluorescence microscopy images of Soy-5 and Soy-9 samples in water, stained with 40 μM ThT at the same experimental conditions. (b) Histogram of the average intensity of ThT fluorescence intensity in the two images. (c) Phasor analysis of FLIM measurements on Soy-5 and Soy-9 samples stained with ThT in water solution. The signal is acquired under laser excitation at 470 nm, in the range 485-630 nm. Data analysis is performed using a double exponential decay whose principal components are $\tau_1 = 0.5$ ns (green) and $\tau_2 = 2.2$ ns (red) identified drawing a straight line interpolating the two lifetime distributions evident in the phasor plot. Lifetime fraction map for the FLIM image colored according to F_1 (fractional contribution of the faster component). Image size is 256x256.

With the idea of using these aggregates as sponge-like structures to purify water from Pb^{2+} ions, we investigated their water accessibility and hydrophobicity, by means of the fluorescent dye Nile Red. Nile Red is an uncharged hydrophobic dye and its fluorescence properties depend on the polarity of the environment in its surroundings. It is known to interact with hydrophobic cavities in native proteins and it is widely used to detect and characterize the exposure or formation of new hydrophobic surfaces during formation of aggregates⁶¹. Specifically, the fluorescence lifetime of this dye is reduced in more polar environments⁶². In Fig. 3, the phasor analysis of FLIM measurements is reported for Nile Red stained samples dispersed in water.

In Fig. 3 a) the phasor plot is shown, where the presence of two lifetime distributions is highlighted by colored circles. Fig 3 b) and c) report the representative 256x256 pixel intensity images acquired for b) Soy-5 sample and c) Soy-9 sample, while in Fig. 3 d) and 3 e) the corresponding lifetime maps are reported. In these images, pixels are colored according to their lifetime in the phasor plot; as a one-to-one correlation exists between the pixels in the image and their phasors, it is possible to select pixels in the phasor plot using a colored circle and they will appear in the same color in the image.

Soy-5 and Soy-9 samples are characterized by two distinguishable fluorescence lifetime distributions in the phasor plot.

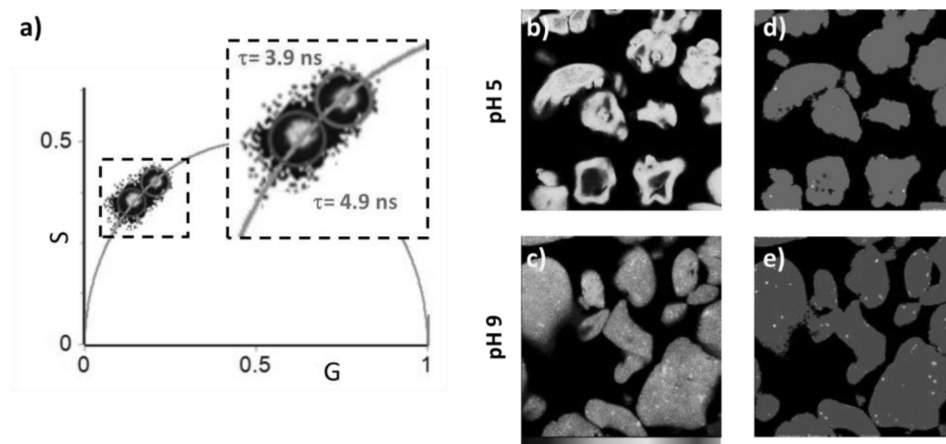


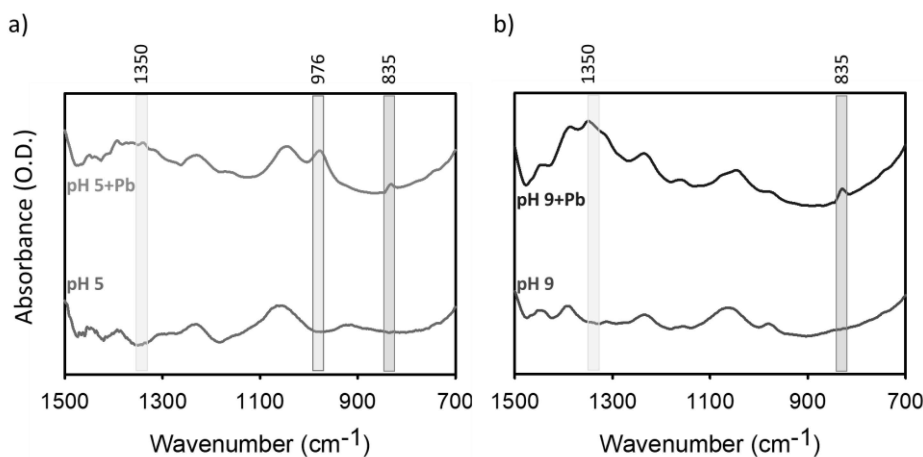
Figure 3. (a-e) Phasor analysis of FLIM measurements on Soy-5 and Soy-9 samples stained using Nile red (60 μ M). The signal was acquired under laser excitation at 540 nm and collected in the range 580-700 nm. (a). Phasor plot showing two different lifetime distributions, highlighted by colored circular cursors. A magnification of the region highlighting the area of interest is reported in the dashed lines surrounded inset. (b-c) Intensity map of Nile Red in (b) Soy-5 sample and (c) Soy-9 sample. (d-e) Lifetime maps corresponding to (b) and (c) measurements respectively, in which the pixels are colored according to the colour cursors used in the phasor plot.

In the present conditions, single exponential decays are observed. Nile Red fluorescence decay with the shorter lifetime (pink cursor: $\tau_i = 3.9$ ns) characterizes the Soy-5 sample whilst in Soy-9 sample the fluorescence decay of the dye is characterized by a longer lifetime (green cursor $\tau_i = 4.9$ ns). Uniform lifetime distribution for Nile red is observed within the same sample despite of inhomogeneity in fluorescence intensity. The shorter lifetime observed in Soy-5 indicates that the hydrophobic binding sites are characterized by higher polarity.

Controversial explanations exist regarding the role of water molecules in metal binding. Some works demonstrated that water molecules might participate in metal binding by stabilizing metals in a particular conformation⁶³. Others, proposed that protein-metal interactions are stronger in media with reduced dielectric constant⁶⁴. In accordance with the latter theory, our result suggests that Soy-9 may present an increased metal binding efficiency.

3.3 Soy microsponges - Pb^{2+} ion interactions studied by Attenuated Total Reflectance-Fourier Transform Infrared (ATR-FTIR) spectroscopy

412 To investigate whether specific interactions exist between Pb^{2+} ions and the soy micronsponges, we
 413 performed ATR-FTIR measurements on freeze dried Soy-5 and Soy-9 samples before and after the
 414 interaction with Pb^{2+} ions. Samples (10-20 mg) were incubated at room temperature and in identical
 415 conditions at room temperature in 20 mL of 30 mg L^{-1} Pb^{2+} metal ions solution for 12 h, then
 416 separated from the solution and freeze dried.
 417 In dried state it is possible to investigate specific spectral regions of interest for protein-metal binding
 418 sites. Fig. 4 a) and b) reports the ATR-FTIR spectra of Soy-5 and Soy-9 samples before and after the
 419 incubation with Pb^{2+} solution. Protein aggregates may contain both specific and not specific metal
 420 binding sites including negatively charged (Asp, Glu) or polar (Cys, His and Asn) residues.
 421 Specifically, it is expected that an attraction between the electron-rich atoms such as O, N and S and
 422 electron-deficient metal ions exists. Thus, thiolate ($-\text{S}-$), carboxylate ($-\text{COO}-$), and amine ($-\text{NH}-$)
 423 groups may be involved in metal binding. By comparing the spectra of both samples before and after
 424 exposure to aqueous solution containing Pb^{2+} ions, variations are observed in the low frequency
 425 spectral region. Both Soy-5 and Soy-9 samples containing Pb^{2+} ions present the growth of two new
 426 peaks at the region around 1350 cm^{-1} (pink region) and 835 cm^{-1} (green region). The peak at about
 427 1350 cm^{-1} is assigned to the specific interaction, generated by the binding between Pb^{2+} ions and the
 428 O-H of the carboxylic acid and C-N of the amino group⁶⁵. The peak at 835 cm^{-1} can be attributed to
 429 interaction of Pb^{2+} ions with S atoms in the polypeptide chain⁶⁶. The interaction of Pb^{2+} ions with the
 430 S atoms of Soy-5 sample is also demonstrated by a pronounced peak at 976 cm^{-1} ^{22,67}.

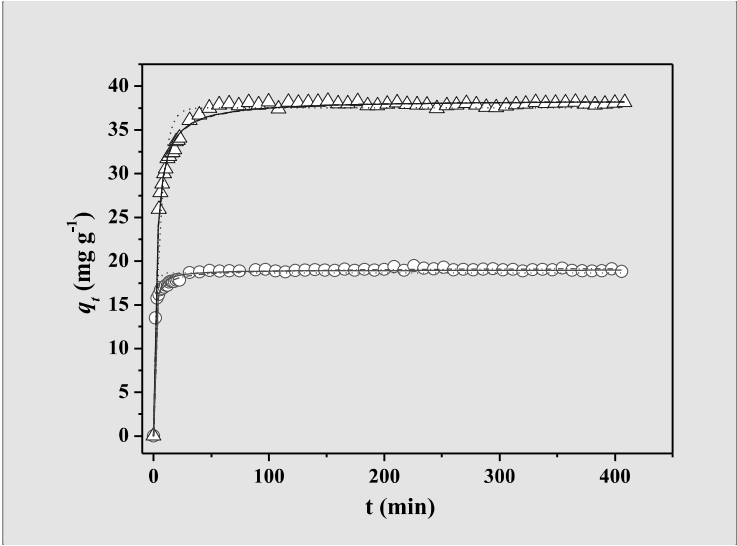


431
 432 **Figure 4.** ATR-FTIR spectra, acquired in the range $1500\text{--}700\text{ cm}^{-1}$, of freeze-dried a) Soy-5 and b) Soy-9
 433 samples before and after the interaction with Pb^{2+} . Colour bands are used to highlight the spectral regions
 434 where significant variations are observed.
 435

436
437
438
439
440
441
442
443

3.4 Kinetics of Pb^{2+} ions adsorption onto Soy microsponges

The kinetics of Pb^{2+} ions adsorption onto Soy-5 and Soy-9 samples have been studied in $NaNO_3$ at $I = 0.1 \text{ mol L}^{-1}$, at $pH = 5$ and at $T = 298.15 \text{ K}$. Only for Soy-9 sample the studies have been extended to $NaCl$ medium at the same experimental conditions. Three kinetic models, namely PFO, PSO and PGO (see Methods section), have been used to fit the experimental data (see Fig. 5 and Fig. SM2 of Supporting Material).



Commentato [v1]: It would be nice to put a legend and to use the same characters as previous figures
Or better to do a single figure with the fig 5 and 6 and table

444
445
446
447
448
449
450
451
452
453
454
455

Figure 5. Dependence of q_t (mg g^{-1}) on contact time for the Pb^{2+} adsorption onto 19.2 mg of Soy-5 sample (\circ) and 11.2 mg of Soy-9 sample (\triangle). Data are fitted with PFO (dotted line) PSO (continuous line), and PGO (dashed/dotted line) kinetic models. Other experimental conditions: 20 mL of aqueous solution containing $NaNO_3$ 0.10 mol L^{-1} ; $Pb(NO_3)_2$ ($c_{Pb^{2+}} = 30 \text{ mg L}^{-1}$), $pH = 5.0$, $T = 298.15 \text{ K}$.

The parameters values of the three kinetic models together with the statistical parameters R^2 and std. dev. values of fits are reported in Table 1, whilst the kinetic parameters values of the best model in terms of goodness of fit are reported in the histograms of Fig. 6.

Table 1. Parameters of PFO, PSO and PGO kinetic equations for Pb^{2+} adsorption on Soy-5 and Soy-9 samples, at $pH = 5.0$, in $NaNO_3$ 0.1 mol L^{-1} and at $T = 298.15 \text{ K}$.

sorbent	PFO parameters		R^2	σ^a
	q_e^b	k_1^c		
Soy-5	18.656 ± 0.095^d	0.686 ± 0.056^d	0.9256	0.7111

Soy-9	37.52 ± 0.20	0.180 ± 0.008	0.9396	1.3782
Soy-9 ^c	27.55 ± 0.18	0.110 ± 0.006	0.9383	1.2005

PSO parameters

	q_e^b	k_2^f		
Soy-5	18.998 ± 0.044	0.0703 ± 0.0034	0.9874	0.2927
Soy-9	38.429 ± 0.081	0.0105 ± 0.0003	0.9923	0.4908
Soy-9 ^c	28.38 ± 0.12	0.0077 ± 0.0004	0.9810	0.6663

PGO parameters

	q_e^b	k_n^g	N		
Soy-5	19.38 ± 0.07	0.017 ± 0.004	2.72 ± 0.11	0.9949	0.1856
Soy-9	38.49 ± 0.15	0.009 ± 0.002	2.040 ± 0.089	0.9922	0.4943
Soy-9 ^c	28.59 ± 0.28	0.005 ± 0.002	2.14 ± 0.15	0.9808	0.6691

^a std. dev of the fit; ^b mg g⁻¹; ^c min⁻¹; ^d \pm std. dev.; ^e in NaCl 0.1 mol L⁻¹; ^f g mg⁻¹ min⁻¹; ^g min⁻¹ (g mg⁻¹)ⁿ⁻¹.

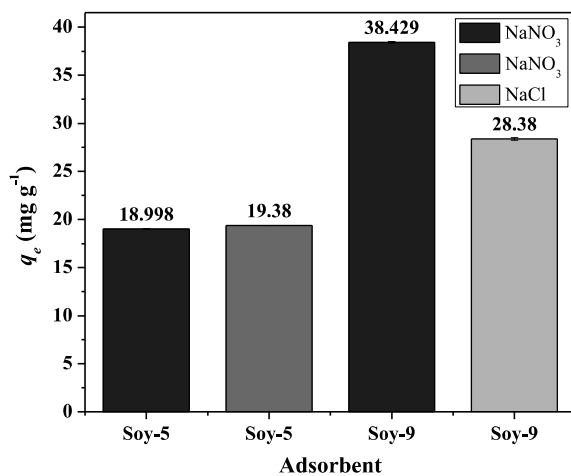


Figure 6. q_e values of PSO (blue or cyan bars) and PGO (magenta bars) kinetic equation for the Pb²⁺ adsorption onto Soy-5 and Soy-9 samples from aqueous solutions containing different ionic media, at $I = 0.1$ mol L⁻¹, at pH = 5.0 and at $T = 298.15$ K.

464 All the adsorbent materials investigated reached the adsorption equilibrium quickly. In particular,
 465 Soy-9 sample needs almost 50 minutes, while Soy-5 sample reaches the adsorption equilibrium within
 466 ~ 25 minutes.

467 Looking at the first two kinetic models considered, the PSO equation fits the experimental data of the
 468 two adsorbent materials better than the PFO (highest R^2 and lowest σ values), suggesting, at least, a
 469 second order kinetics of Pb^{2+} adsorption. Extending the analysis to the third kinetic model, the
 470 statistical parameters values of the fits show that also the PGO model fits quite well with the
 471 experimental data. For this reason, additional comments based on the kinetic parameters derived from
 472 the PGO equation can be made.

473 The PGO model has been already used by several authors^{68–70}. Unlike the other two models, the PGO
 474 equation provides a non-predetermined reaction order (n). The reaction order is closely related to the
 475 characteristics of the adsorbent (structure, conformation, number and type of available binding sites)
 476 as well as to the experimental conditions of the adsorbent – metal ion system, such as ionic medium,
 477 ionic strength, and pH that influence all the aforementioned adsorbent characteristics. The intrinsic
 478 properties of protein microsponges suggest an increase of adsorption sites available to bind the metal
 479 ion. These sites include specific amino acidic sidechains, the already present binding sites in the
 480 native soy protein isolate, typical of amyloid structures, and new hydrophobic cavities that could be
 481 responsible of a kinetic order of adsorption higher than two^{69,70}. The refined n value obtained for Soy-
 482 9 in $NaNO_3$ medium is 2.04. This value is higher if compared with the pseudo-first order previously
 483 found for Soy protein hollow microspheres,¹⁰ confirming that the structural characteristic of the
 484 adsorbent and the experimental conditions are crucial¹⁰.

485 Moreover, considering the experimental errors, comparable values of kinetic constants have been
 486 calculated by PSO and PGO models in this ionic medium (see Table 1). This means that for the Pb^{2+}
 487 ions adsorption onto Soy-9 protein microsponges the PGO and PSO models are equivalent,
 488 confirming a pseudo second order kinetic of adsorption. The comparable n and k_n values calculated
 489 for Soy-9 sample in $NaNO_3$ and $NaCl$ media indicate that the kinetic of adsorption is not influenced
 490 by the ionic composition of the metal ion solution. On the contrary, the ionic medium composition
 491 affects the adsorption ability of the adsorbent at equilibrium, which decreases in $NaCl$ ($q_e = 38.49$
 492 and 28.59 mg g^{-1} in $NaNO_3$ and $NaCl$, respectively). This is probably due to the formation of lead-
 493 chloride species that changes the chemical speciation profile of the metal ion reducing the percent of
 494 Pb^{2+} ions in solution.

495 The statistical testing parameters (R^2 and std. dev. of fit) values indicate the PGO model as the best
 496 fit for Soy-5 sample. Moreover, the kinetic constant (k_n) and the reaction order n calculated do not
 497 agree with those refined (k_2) or fixed (2) in the PSO model. In particular, different constant ($k_n =$

498 0.005 min⁻¹ (g mg⁻¹)ⁿ⁻¹) and reaction order ($n = 2.72$) have been calculated. This indicates that the
499 kinetics of metal ion uptake by Soy-5 sample are more complex as they have a fractional reaction
500 order higher than 2.

501 The adsorption kinetics of Soy-5 is comparable with that previously reported for the adsorption of
502 the same metal ion onto amyloid particulates of BSA at the same pH, toxic metal ion concentration
503 and ionic strength²² this confirming that generic features of protein molecule may regulate Pb²⁺
504 uptake. Specifically, BSA particulates, like Soy-5, adsorbed Pb²⁺ ions following kinetics of pseudo
505 general order model with a refined reaction order value between 2.75 and 3.14. The lower kinetic
506 order of Pb²⁺ ions adsorption onto Soy-9 ($2.084 \leq n \leq 2.14$) is presumably attributable to the less
507 packed organization of β -structures in the Soy-9 sample (see section 3.2).

508 Under the experimental conditions of the kinetic experiments, the equilibrium adsorption capacities
509 (q_e) of the microsponges in NaNO₃ 0.1 mol L⁻¹ have the following trend: Soy-9 sample > Soy-5 sample
510 (see Fig. 6). This indicates that the observed differences in the structures of SPI microsponges,
511 obtained only by incubating the protein isolate at two different pH in aqueous solution, play an
512 important role on the performance of the adsorbent material. In particular, the q_e of protein sample
513 increases for SPI microsponges produced at pH 9. However, this is only a rough estimate considering
514 the different amounts of Soy-5 and Soy-9 samples used in the kinetic experiments (~ 19 mg of Soy-
515 5 sample and ~ 11 mg of Soy-9 sample). This aspect will be discussed in detail in the next section.

516

Commentato [v2]: Non può dipendere anche dal binding site in più?

517 3.5 Adsorption equilibria of Pb^{2+} ions onto Soy microsponges

518 The thermodynamics of Pb^{2+} ion adsorption onto SPI microsponges have been studied through a
519 series of batch adsorption experiments at different experimental conditions, namely pH range 4.0 –
520 6.5, without ionic medium or with the addition of $NaNO_3$ or $NaCl$, at different ionic strengths (0.10
521 $\leq I / \text{mol L}^{-1} \leq 0.50$), and at $T = 298.15 \text{ K}$. The experimental data were then processed with the
522 Langmuir and Freundlich isotherm models. The parameters of the models were subsequently
523 analyzed in order to obtain information regarding the maximum adsorption capacities and affinities
524 of Soy microsponges towards the toxic metal ion. The fitting curves of the experimental data (q_e vs
525 c_e) using Langmuir and Freundlich isotherm equations are depicted in Fig. 7 and in Fig. SM3 – SM5
526 of Supplementary Material.

527 The values of the parameters of the two isotherm equations are reported in Tables 2 and 3 together
528 with the statistical parameters of fits R^2 and σ and in the histograms of Fig. 8 and 9 for an easier
529 comparison. Both models fitted quite well the experimental data, though in most cases the fits with
530 Langmuir model showed a slightly higher R^2 and lower σ .

531 A first set of batch experiments was carried out to study the adsorption equilibria of Pb^{2+} /Soy-5, and
532 Pb^{2+} /Soy-9 systems at the same experimental conditions ($c_{Pb^{2+}} \approx 30 \text{ mg L}^{-1}$, $pH = 5$, $NaNO_3$ medium,
533 $I = 0.1 \text{ mol L}^{-1}$ and $T = 298.15 \text{ K}$) with the aim to establish which of the prepared protein microsponges
534 was the best adsorbent of Pb^{2+} ions.

535 The results of adsorption isotherms substantially confirm the q_e trend obtained through kinetic
536 experiments at a single adsorbent/metal ion ratio. Specifically, both the maximum adsorption capacity
537 (q_m) and affinity (K_L) are larger for Soy-9 sample with respect to Soy-5, reaching the q_m value of
538 37.74 mg g^{-1} and a K_L equal to 0.97 L mg^{-1} for Soy-9 sample (see Fig. 8).

539 The balance between specific binding sites, which are diversified in the two samples (see Fig. 4),
540 different water accessibility, and polarity of the internal cavities contribute to the observed different
541 behaviour.

542 Structural and physicochemical properties of the samples have to be taken into account to explain this
543 difference. Indeed, as shown in previous sections, the two adsorbents not only differ in the molecular
544 structure, but also in the polarity of accessible cavities, with Soy-5 sample being characterized by a
545 higher polarity. Soy-9 sample presents the typical amyloid peak centred at 1620 cm^{-1} in FTIR
546 spectrum, indicating the presence of a significant amount of parallel intermolecular β structure (35
547 %), whilst antiparallel β structures are present in lower amount. Soy-5 sample presents a more
548 heterogeneous structure where strong intermolecular β -sheet (16 %) are also present, possibly with
549 reduced intermolecular distances between strands. This may change water accessibility and,
550 consequently, metal accessibility to the internal parts of the aggregates. In addition, the whole Soy-5

microsponges structures are characterized by a higher polarity in water and this may affect the affinity. In line with that, we have previously suggested that protein and metal hydration water may play a significant role in Pb^{2+} ions adsorption from protein aggregates²²; local interactions between water molecules and the polar and nonpolar regions in protein may modify protein hydration thus regulating occurring interactions⁶³. Indeed, water molecules may also participate in metal binding and stabilize the metals in a particular conformation⁵⁹.

At this point, investigation on Soy-9 has been extended to other experimental conditions changing the pH, the ionic medium and the ionic strength of the Pb^{2+} aqueous solutions.

Experimental conditions of the toxic metal ion solution can critically affect the adsorption performances of the adsorbent material used in decontamination treatments for several reasons: i) low pH values can cause partial or total protonation of binding groups of the protein microsponges ($-\text{COOH}$, $-\text{NH}_2$, $-\text{SH}$) as well as high pH values lead to the formation of hydrolytic species of Pb^{2+} ions ($\text{Pb}(\text{OH})^+$, $\text{Pb}(\text{OH})_2$, $\text{Pb}(\text{OH})_3^-$ and other polynuclear hydrolytic species not present at the Pb^{2+} concentrations used in this work); ii) the ions coming from the ionic medium dissociation could form ion pairs or weak complexes with some of the binding groups of the adsorbent as well as with the Pb^{2+} ions (PbCl^+ , PbCl_2 , PbCl_3^- , $\text{PbCl}(\text{OH})$); moreover they can produce adsorbent modifications; iii) the increase of ionic strength, mainly related to the ionic medium concentration, enhances the background salt effects listed in previous point⁷¹⁻⁷³.

The adsorption isotherm of Pb^{2+} ions onto Soy-9 sample at $\text{pH} = 4$ showed an unusual trend (see Fig. SM4 a)). In fact, at a fixed metal ion concentration ($c_{\text{Pb}^{2+}} \approx 30 \text{ mg L}^{-1}$), the adsorption capacity of the protein microsponges, at first, increases as the amount of Soy-9 sample decreases, reaching a maximum and then rapidly going to zero. This anomalous trend can be attributed to structural modifications and destabilisation of the protein microsponges. Indeed, a subtle interplay between long range electrostatic forces, hydrophobic interactions and short-range protein - protein interactions is involved in the stability of protein aggregates. The pH value of 4 is critically different from the pH in which the Soy-9 aggregates are formed and, in particular, is on the opposite side with respect to the isoelectric point. As previously reported^{74,75}, by inverting the protein charge it is likely that the electrostatics interactions involved in β -structure stabilization are critically modified leading to aggregates disruption. This is also confirmed by the difficulties encountered during the voltammetric experiments carried out on metal ion solutions post adsorption. In fact, due to the release in solution of degradation products of soy proteins, at this pH value, a more accurate cleaning of electrodes was mandatory between measurements due to a particularly adhesiveness of substances released by the Soy 9 sample to the electrodes of the voltammetric cell.

584 A “regular” adsorption behaviour was obtained at $\text{pH} \geq 5$, i.e. above protein pI, as shown in Fig. SM4
 585 b) and c). This indicates that Soy-9 sample can be regularly used for Pb^{2+} ions decontamination of
 586 wastewaters, the pH of which is not less than 5. The adsorption capacity of Soy-9 increases with the
 587 increase of pH ($q_m = 37.74$ and 56.2 mg g^{-1} at pH 5.0 and 6.5, respectively). Looking at the Pb^{2+}
 588 speciation profile obtained with literature formation constants of hydrolytic species in NaClO_4
 589 (formation constants in this ionic medium can be compared to those in NaNO_3 considering that both
 590 are non-interacting media toward Pb^{2+})^{76,77}, the formation percentage of Pb^{2+} aquo ion goes from 100
 591 % to 95 % when the pH passes from 5.0 to 6.5. Considering that the remaining 5 % consists of the
 592 positively charged $\text{Pb}(\text{OH})^+$ species, the increasing of q_m is not attributable to relevant changes in
 593 Pb^{2+} chemical speciation and can be explained as follow: i) at pH = 6.5, the competition between H^+
 594 and Pb^{2+} ions for the binding sites of Soy-9 sample is lower; ii) at this pH, the binding sites of protein
 595 aggregate are almost deprotonated and, therefore, more available to bind the toxic metal ion.
 596 Moreover, at pH = 5, i.e. close to the protein pI, electrostatic interactions are likely to be negligible
 597 while at pH = 6.5, i.e. above the pI, the electrostatic attraction between Pb^{2+} ions and the negatively
 598 charged microsponges surface may be a relevant factor leading to increased metal adsorption.
 599 The ionic medium affects the adsorption capacity of Soy-9 sample and its effect depends on the type
 600 of ions coming from its dissociation. This assumption is confirmed by the q_m values obtained without
 601 ionic medium, in NaNO_3 0.1 mol L^{-1} and in NaCl at the same ionic strength. The differences between
 602 the q_m values obtained at $I \rightarrow 0 \text{ mol L}^{-1}$ and in NaNO_3 0.1 mol L^{-1} are within the experimental error
 603 ($q_m = 36.40$ and 37.74 without ionic medium and in NaNO_3 0.1 mol L^{-1} , respectively), whilst the
 604 addition of NaCl 0.1 mol L^{-1} reduces the adsorption capacity of the adsorbent by about 7 mg g^{-1} .
 605 Although the addition of NaNO_3 would appear to be irrelevant, a 5-fold increase of its concentration
 606 reduces the adsorption capacity of Soy-9 sample although the effect of NaNO_3 is always lower than
 607 that of NaCl ($q_m = 22.6$ and 11.6 mg g^{-1} at $I = 0.5 \text{ mol L}^{-1}$ in NaNO_3 and NaCl , respectively) (see
 608 histogram of Fig. 9 a)).
 609 In Fig. SM6 a comparison is depicted between the sum of percentages of positively charged species
 610 of Pb^{2+} ions in solution (Σ^+) and the q_m values of Soy-9 sample as function of ionic strength in NaCl
 611 and NaClO_4 or NaNO_3 . The comparison of Σ^+ and of q_m values provides useful information
 612 considering that the interaction between lead and the functional groups of the adsorbent mainly
 613 involves the positively charged species of the metal ion.
 614 Independently of the ionic strength value, at pH = 5 and in NaClO_4 , a non-interacting medium like
 615 NaNO_3 , the Σ^+ is 100 % like in absence of ionic medium ($I \rightarrow 0 \text{ mol L}^{-1}$). This justifies the unvaried
 616 q_m value of Soy-9 sample with the addition of NaNO_3 0.1 mol L^{-1} to the metal ion solution. Moreover,
 617 the reduction of q_m in NaNO_3 0.5 mol L^{-1} , considering the unvaried Pb^{2+} speciation profile, can be

explained in terms of competition of Na^+ ions towards binding sites of protein microsponges and/or in terms of shielding/shrinking effect on the microsponges caused by the ions of the more concentrated ionic medium and consequent reduction of available binding.

The gradual and higher q_m reduction observed with the increasing of NaCl concentration can be explained, as for NaNO_3 , by competing and/or shielding effects of the ions coming from NaCl dissociation; in addition, a significant reduction of Σ^+ ($\Sigma^+ = 100$ and 49.7 % at $\text{pH} = 5.0$, at $I \rightarrow 0$ mol L^{-1} and in NaCl 0.5 mol L^{-1} , respectively) must be considered in the explanation.

The presence of ionic medium in the Pb^{2+} ions solution reduces also the affinity (K_L values) of the adsorbent material towards the target metal ion, but, unlike q_m , the effect of NaCl and NaNO_3 , considering the experimental errors, is equivalent ($K_L = 0.768$, 0.40 and 0.46 L mg^{-1} without ionic medium, in NaNO_3 0.5 mol L^{-1} and in NaCl 0.5 mol L^{-1} , respectively) (see histogram of Fig. 9 b)).

The results of adsorption isotherms reflect the trend of the ΔpH values, i.e. the mean difference between the pH at adsorption equilibrium and that of solution before adsorption ($\text{pH}_f - \text{pH}_i$) measured in each batch of each adsorption experiment (see Tables 2 and 3).

At $\text{pH}_i = 5.0$, in absence of background salt and in NaNO_3 , the ΔpH is ~ 0.6 , whilst, in NaCl it gradually increases with increasing of ionic strength going from 0.7 in NaCl 0.05 mol L^{-1} to 1.07 in NaCl 0.5 mol L^{-1} . The increase of solution pH at the end of the experiments is presumably due to the protonation of some functional groups of the protein aggregate. Indeed, at $\text{pH}_i = 5.0$, the H^+ ions of solution compete with the Pb^{2+} ions towards binding groups of the adsorbent material. The competition of H^+ ions is more significant in NaCl in which the formation of chloride species of Pb^{2+} , that gradually increases with the increase of NaCl concentration, reduces the percentage of positively charged species of the metal ion. At $\text{pH}_i = 6.5$ the H^+ competition is reduced and Pb^{2+} ions are adsorbed to the Soy-9 sample also replacing the proton of some protonated sites causing the pH reduction ($\Delta\text{pH} = -0.62$).

In the plethora of scientific articles concerning the adsorption of toxic metals from polluted waters, only a recent paper concerns the use of adsorbents based on or enriched with amyloid structures^{22,78–80}. An example of hybrid material formed by protein amyloid fibrils of sunflower and peanut meals coupled with carbon membranes was proposed by Soon et al. in 2022⁸¹. This material removed efficiently heavy metals, including lead, from water solutions and its q_m values are of the same order of magnitude of those found for Soy-5 and Soy-9 microsponges presented in this work.¹⁰ Also Yang et al.⁸⁰ demonstrated the excellent metal sorption ability of a protein-based hybrid material formed by bovine serum albumin, tris(2-carboxyethyl) phosphine and sodium carboxymethyl cellulose (PTB/CMC). However, in our previous work²² we demonstrated that, despite the different experimental conditions, amyloid particulates, based only on BSA can present comparable or better

652 adsorption ability than hybrid materials. Furthermore, our data underline the fact that in addition to
653 the metal ion binding sites, intrinsically present in the originating protein, the 3D structure, of the
654 BSA particulates²² before and of Soy-5 and Soy-9 microsponges now, is crucial for the metal binding
655 ability. Importantly, the low cost and high abundance of SPI place it in the forefront as an excellent
656 alternative biomaterial to the amyloid adsorbents already proposed.

657
658
659

Table 2. Freundlich and Langmuir isotherm parameters for the Pb^{2+} adsorption onto Soy-5 and Soy-9 samples from Pb^{2+} ($c_{\text{Pb}}^{2+} = 30 \text{ mg L}^{-1}$) aqueous solutions at $\text{pH} = 5.0$, in NaNO_3 0.10 mol L^{-1} and at $T = 298.15 \text{ K}$.

Adsorbent	pH _i ^a	pH _f ^a	Langmuir parameters			Freundlich parameters				
			q_m^b	K_L^c	R ²	σ ^d	K _F ^e	n	R ²	σ ^d
Soy-5	5.02	4.93	23.16 ± 0.61 ^f	0.386 ± 0.033 ^f	0.9945	1.3712	8.75 ± 0.25 ^f	3.02 ± 0.14 ^f	0.9961	0.9714
Soy-9	5.00	5.61	37.74 ± 0.72	0.97 ± 0.15	0.9863	14.1018	25.7 ± 1.7	9.1 ± 2.0	0.9643	36.760

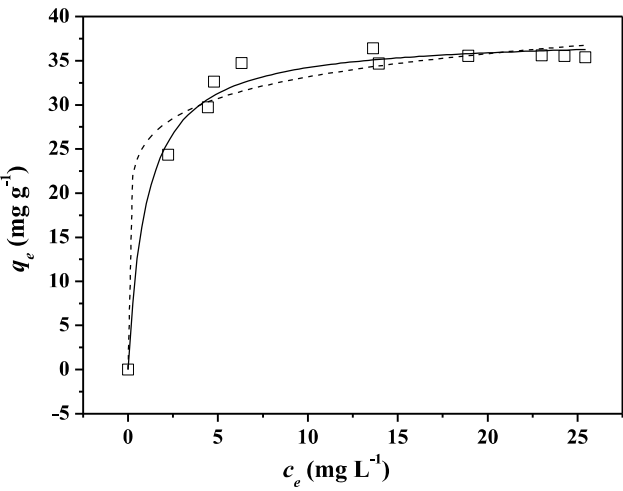
^a mean values of initial and final pH of Pb^{2+} solutions used in isotherm experiments; ^b in mg g^{-1} ; ^c in L mg^{-1} ; ^d std. dev of the fit; ^e $\text{L}^{1/n} \text{g}^{-1} \text{mg}^{1-1/n}$; ^f \pm std. dev.

Table 3. Freundlich and Langmuir isotherm parameters for the Pb^{2+} adsorption onto Soy-9 sample from Pb^{2+} ($c_{\text{Pb}}^{2+} = 30 \text{ mg L}^{-1}$) aqueous solutions containing different ionic media, at different ionic strengths and pH and at $T = 298.15 \text{ K}$.

Medium	$I / mol\ L^{-1}$	pH_i^a	pH_f^a	Langmuir parameters				Freundlich parameters			
				q_m^b	K_L^c	R^2	σ^d	K_F^e	n	R^2	σ^d
-	$\rightarrow 0$	4.95	5.50	36.40 ± 0.53^f	0.768 ± 0.093^f	0.9858	1.2444	21.3 ± 1.9^f	6.9 ± 1.3^f	0.9293	2.7761
NaNO ₃	0.10	5.00	5.61	37.74 ± 0.72	0.97 ± 0.15	0.9863	14.1018	25.7 ± 1.7	9.1 ± 2.0	0.9643	36.760
NaNO ₃	0.10	6.54	5.92	56.2 ± 2.1	0.211 ± 0.036	0.9726	2.2903	23.9 ± 2.3	4.88 ± 0.74	0.9653	2.5757
NaNO ₃	0.50	4.95	5.53	22.6 ± 3.2	0.40 ± 0.16	0.9676	1.0512	8.05 ± 1.30	2.57 ± 0.69	0.9605	1.1597
NaCl	0.05	4.99	5.69	33.18 ± 0.61	0.92 ± 0.13	0.9919	0.8680	21.7 ± 1.3	7.6 ± 1.4	0.9806	1.3401
NaCl	0.10	4.99	5.72	29.8 ± 1.3	0.62 ± 0.17	0.9763	1.4267	18.1 ± 1.5	7.1 ± 1.6	0.9750	1.4660
NaCl	0.30	4.98	5.92	16.57 ± 0.53	0.677 ± 0.076	0.9920	0.3981	6.75 ± 0.35	2.51 ± 0.22	0.9808	0.6188
NaCl	0.50	4.97	6.04	11.6 ± 1.7	0.46 ± 0.14	0.9582	0.4972	3.65 ± 0.32	1.84 ± 0.30	0.9345	0.6223

^a mean values of initial and final pH of Pb^{2+} solutions used in isotherm experiments; ^b in mg g^{-1} ; ^c in L mg^{-1} ; ^d std. dev of the fit; ^e $\text{L}^{1/n} \text{g}^{-1} \text{mg}^{1-1/n}$; ^f \pm std. dev.

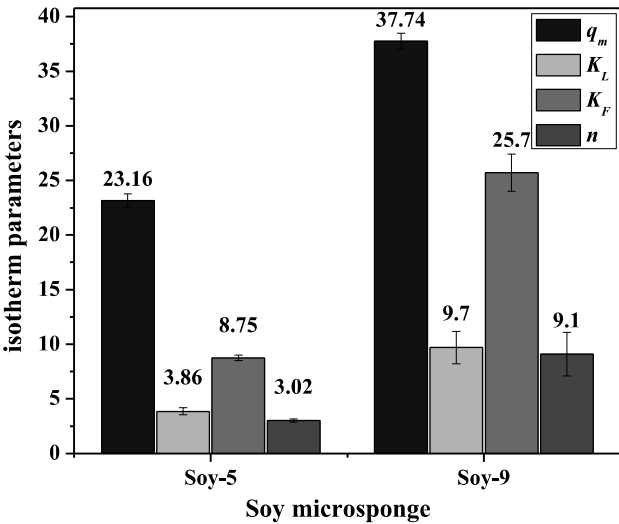
668



669

670 **Figure 7.** Adsorption isotherm of Pb^{2+} onto Soy-9 sample from aqueous solutions containing NaNO_3 0.10 mol
671 L^{-1} , at $\text{pH} = 5.00$ and $T = 298.15$ K. Experimental data fitted with Freundlich (dashed lines) and Langmuir
672 (continuous lines) isotherm equations.
673
674

675



676

677

678

679

680

681

682

Figure 8. Langmuir and Freundlich parameters values for the Pb^{2+} ion adsorption onto Soy-5 and Soy-9 microsponges from aqueous solutions containing NaNO_3 0.1 mol L^{-1} , at $\text{pH} = 5.0$ and $T = 298.15 \text{ K}$.

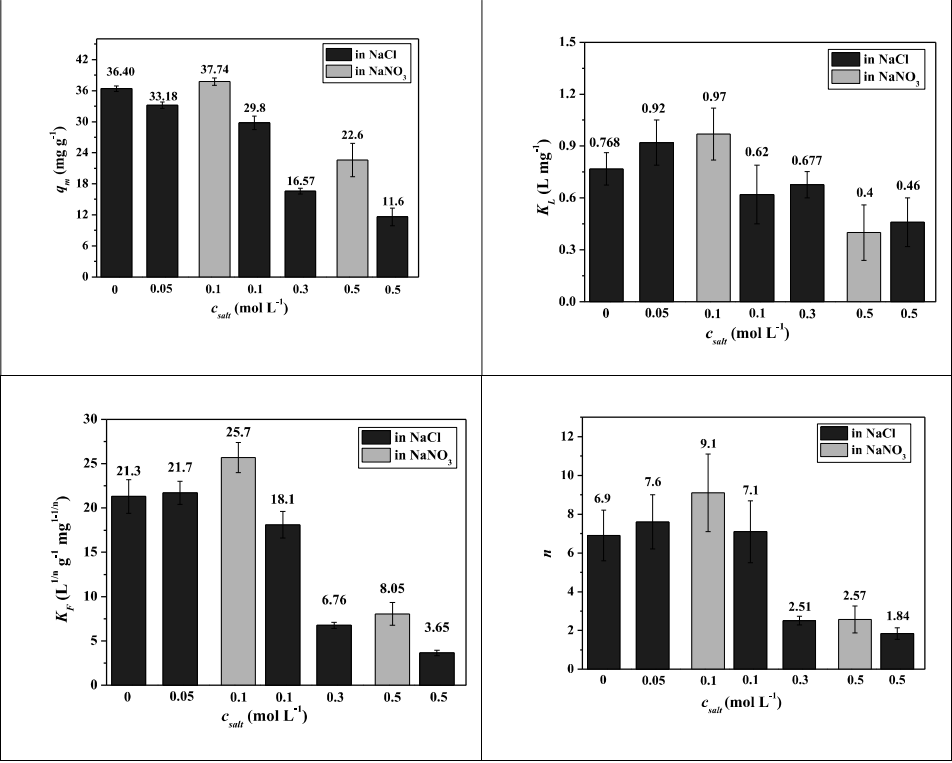


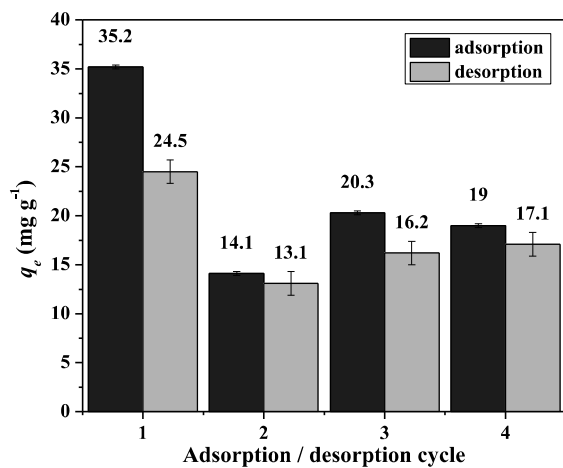
Figure 9. Effect of ionic medium and of ionic strength on the Langmuir parameters q_m (a) and K_L (b) and on Freundlich parameters K_F (c) and n (d) for the Pb^{2+} ion adsorption onto Soy-9 sample. Other experimental details of metal ion solution: pH = 5.0, $T = 298.15$ K.

3.4 Recycle and reuse of Soy-9 sample.

The adsorbent recycling is a very important aspect of environmental decontamination processes. Indeed, the possibility of reusing the same material n times proportionally reduces the costs of the process. Thus, recycle and reuse experiments have been carried out with Soy-9 sample, the best adsorbent material towards Pb^{2+} ions, making four adsorption/desorption cycles (see section 2.4 for experimental details). The results, in terms of q_e of adsorption and desorption of the four cycles are depicted in the histogram reported in Fig. 10.

The Soy-9 sample showed a good reuse capacity. In particular, in the first cycle the q_e of adsorption reach the 35.2 mg g^{-1} . In the next three adsorption / desorption cycles the adsorption ability of the adsorbent decreases of $\sim 40 \%$ and, with some small fluctuation, remains almost constant.

699 The recovered metal ion in the first desorption step is lower than the adsorbed one ($q_{e \text{ adsorption}} - q_{e \text{ desorption}} = 10.7 \text{ mg g}^{-1}$), whilst, starting from the second cycle, the amount of Pb^{2+} ion adsorbed and
 700 desorbed are comparable. This could be the reason of the lowering of adsorption ability of the
 701 adsorbent material after the first cycle. Indeed, part of the metal ion adsorbed in the first adsorption
 702 step is likely covalently bounded to the adsorbent and the EDTA solution is not able to extract it.
 703 Another explanation could be the partial degradation of Soy-9 sample during the reuse experiments.
 704
 705



706
 707 **Figure 10.** q_e values of adsorption / desorption steps. Experimental details: amount of Soy-9 sample $\approx 5 \text{ mg}$;
 708 metal ion solution: 15 mL of Pb^{2+} ($c_{\text{Pb}^{2+}} \approx 30 \text{ mg L}^{-1}$), $\text{pH} = 5.0$, in NaNO_3 0.1 mol L^{-1} and $T = 298.15 \text{ K}$;
 709 extractant solution: 15 mL of EDTA 0.10 mol L^{-1} .
 710

711 4. Conclusions

712 We have presented a quantitative study on the successful production of highly efficient SPI-based
 713 microsponges for water purification application. The material is entirely composed of the plant-based
 714 SPI and is fabricated by a simple and scalable production procedure with minimal use of chemical
 715 reagents. This results in an environmentally-sustainable and low-cost platform, matching the basic
 716 principles of green chemistry.

717 Our SPI microsponges successfully removed Pb^{2+} ions from aqueous environments, also
 718 demonstrating a high degree of recycling in terms of multiple use of the same composite matrix.
 719 Subtle variations of the production conditions translated into substantially different performance of
 720 the materials. Specifically, by simply changing the pH of the solution, from the isoelectric point (pH

Commentato [KK3]: I'm not sure whether we can call it a platform

5) to a pH where proteins are highly charged (pH 9), we obtained micron-sized aggregates with different content of intermolecular β -structures and internal polarity, which presented a certain ability in removing Pb^{2+} ions from water at pH values above protein isoelectric point ($> pH\ 5$), making these materials suitable for drinking and waste water purification.

The fact that the sample grown at pH 5 presented a lower affinity with respect to the one grown in solution at pH 9 allowed us to highlight general properties of protein aggregates, which may regulate metal sorption. We showed that specific interaction occurs between O-H of the carboxylic acids and C-N of the amino groups and cysteines for both samples. However, interestingly, Soy-5 sample, which has a lower affinity for Pb^{2+} , presents in the IR spectrum a supplementary fingerprint of a specific binding site ($976\ cm^{-1}$) which may be attributed to specific electrostatic interactions with protein. In addition to the latter, also hydrophobic interactions and hydrogen bonding appeared to be significantly involved in metal binding. Furthermore, although both samples present intermolecular β -structures typical of amyloids, the sample with higher level of order and hydrophobicity is characterized by an enhanced metal binding affinity. This suggests that water molecules are important players in regulating the metal binding efficiency and in particular our data suggest that the binding efficiency is hindered in media with increased dielectric constant.

Author Contributions

Sara Anselmo: Investigation, Formal analysis, Methodology, writing – review & editing, Data curation, Visualization. **Tiziana Avola:** Investigation, Formal analysis, Methodology, Data curation, Visualization. **Kleopatra Kalouta:** Investigation, Formal analysis, Methodology, writing – review & editing, Data curation, Visualization. **Salvatore Cataldo:** Investigation, Data Curation. **Giuseppe Sancataldo:** Investigation, Visualization, Writing – review & editing. **Nicola Muratore:** Investigation, Methodology, Data Curation. **Vito Foderà:** Conceptualization, Supervision, Project administration, Funding acquisition, Writing – review & editing, Resources. **Alberto Pettignano:** Conceptualization, Methodology, Data Curation, Validation, Investigation, Formal analysis, Supervision, writing – original draft, Writing – review & editing. **Valeria Vetri:** Conceptualization, Methodology, Validation, Investigation, Formal analysis, Supervision, writing – original draft, Writing – review & editing, Project administration, Funding acquisition, Resources.

ACKNOWLEDGMENTS

The authors thank the University of Palermo for financial support (FFR – PROMETA project). The VILLUM FONDEN is also acknowledged for funding – Villum Young Investigator Grant “Protein superstructure as Smart Biomaterials (ProSmart)” 2018-2023 (project number: 19175).

Commentato [v4]: E porta a una cinetica del terzo ordine?

REFERENCES

1. Mearns 1 ' AJ, Reish DJ, Oshida PS, et al. Effects of Pollution on Marine Organisms. *Water Environment Research*. 2014;86(10):1869-1954. doi:10.2175/106143014X1403L280668498
2. Goel PK. Water pollution : causes, effects and control. Published online 1997:269.
3. Montgomery AA, Elimelech M. Millions suffer from preventable illnesses and die every year. Published online 2007.
4. Transforming our world: the 2030 Agenda for Sustainable Development | Department of Economic and Social Affairs. Accessed August 2, 2022. <https://sdgs.un.org/2030agenda>
5. Liu X. Research Progress on Treatment Technology of Produced Water by Adsorption Method. *IOP Conf Ser Mater Sci Eng*. 2019;472(1). doi:10.1088/1757-899X/472/1/012082
6. Aziz HA, Adlan MN, Ariffin KS. Heavy metals (Cd, Pb, Zn, Ni, Cu and Cr(III)) removal from water in Malaysia: Post treatment by high quality limestone. *Bioresour Technol*. 2008;99(6):1578-1583. doi:10.1016/J.BIORTECH.2007.04.007
7. Nalaparaju A, Jiang J. Ion exchange in metal-organic framework for water purification: Insight from molecular simulation. *Journal of Physical Chemistry C*. 2012;116(12):6925-6931. doi:10.1021/JP210082F
8. ZHANG L, WU Y, QU X, LI Z, NI J. Mechanism of combination membrane and electro-winning process on treatment and remediation of Cu²⁺ polluted water body. *Journal of Environmental Sciences*. 2009;21(6):764-769. doi:10.1016/S1001-0742(08)62338-4
9. Ahmadi A, Wu T. Towards full cell potential utilization during water purification using Co/Bi/TiO₂ nanotube electrodes. *Electrochim Acta*. 2020;364:137272. doi:10.1016/J.ELECTACTA.2020.137272
10. Liu D, Li Z, Li W, et al. Adsorption behavior of heavy metal ions from aqueous solution by soy protein hollow microspheres. *Ind Eng Chem Res*. 2013;52(32):11036-11044. doi:10.1021/IE401092F/ASSET/IMAGES/MEDIUM/IE-2013-01092F_0009.GIF
11. QU J. Research progress of novel adsorption processes in water purification: A review. *Journal of Environmental Sciences*. 2008;20(1):1-13. doi:10.1016/S1001-0742(08)60001-7
12. Popuri SR, Vijaya Y, Boddu VM, Abburi K. Adsorptive removal of copper and nickel ions from water using chitosan coated PVC beads. *Bioresour Technol*. 2009;100(1):194-199. doi:10.1016/J.BIORTECH.2008.05.041
13. Xu X, Hao R, Xu H, Lu A. Removal mechanism of Pb(II) by *Penicillium polonicum*: immobilization, adsorption, and bioaccumulation. *Scientific Reports* 2020 10:1. 2020;10(1):1-12. doi:10.1038/s41598-020-66025-6
14. Demey H, Vincent T, Guibal E. A novel algal-based sorbent for heavy metal removal. *Chemical Engineering Journal*. 2018;332:582-595. doi:10.1016/J.CEJ.2017.09.083
15. Halttunen T, Salminen S, Tahvonen R. Rapid removal of lead and cadmium from water by specific lactic acid bacteria. *Int J Food Microbiol*. 2007;114(1):30-35. doi:10.1016/j.ijfoodmicro.2006.10.040
16. Halttunen T, Salminen S, Tahvonen R. Rapid removal of lead and cadmium from water by specific lactic acid bacteria. *Int J Food Microbiol*. 2007;114(1):30-35. doi:10.1016/J.IJFOODMICRO.2006.10.040

17. Bansal M, Garg U, Singh D, Garg VK. Removal of Cr(VI) from aqueous solutions using pre-consumer processing agricultural waste: A case study of rice husk. *J Hazard Mater.* 2009;162(1):312-320. doi:10.1016/J.JHAZMAT.2008.05.037
18. Atia AA, Donia AM, Abou-El-Enein SA, Yousif AM. Studies on uptake behaviour of copper(II) and lead(II) by amine chelating resins with different textural properties. *Sep Purif Technol.* 2003;33(3):295-301. doi:10.1016/S1383-5866(03)00089-3
19. Nasrollahzadeh M, Sajjadi M, Iravani S, Varma RS. Starch, cellulose, pectin, gum, alginate, chitin and chitosan derived (nano) materials for sustainable water treatment: A review. *Carbohydr Polym.* 2021;251:116986. doi:10.1016/J.CARBPOL.2020.116986
20. Cataldo S, Gianguzza A, Pettignano A. Sorption of Pd(II) ion by calcium alginate gel beads at different chloride concentrations and pH. A kinetic and equilibrium study. Published online 2016. doi:10.1016/j.arabjc.2014.10.031
21. Cataldo S, Gianguzza A, Pettignano A, Villaescusa I. Mercury(II) removal from aqueous solution by sorption onto alginate, pectate and polygalacturonate calcium gel beads. A kinetic and speciation based equilibrium study. *React Funct Polym.* 2013;73(1):207-217. doi:10.1016/j.reactfunctpolym.2012.10.005
22. Anselmo S, Cataldo S, Avola T, et al. Lead(II) ions adsorption onto amyloid particulates: An in depth study. *J Colloid Interface Sci.* 2021;610:347-358. doi:10.1016/J.JCIS.2021.11.184
23. Bolisetty S, Mezzenga R. Amyloid-carbon hybrid membranes for universal water purification. *Nat Nanotechnol.* 2016;11(4):365-371. doi:10.1038/NNANO.2015.310
24. Vandenbossche M, Jimenez M, Casetta M, Traisnel M. Remediation of Heavy Metals by Biomolecules: A Review. <http://dx.doi.org/10.1080/106433892014966425>. 2015;45(15):1644-1704. doi:10.1080/10643389.2014.966425
25. Shen Y, Levin A, Kamada A, et al. From Protein Building Blocks to Functional Materials. *ACS Nano.* 2021;15(4):5819-5837. doi:10.1021/ACS.NANO.0C08510
26. Vetri V, Piccirilli F, Krausser J, et al. Ethanol Controls the Self-Assembly and Mesoscopic Properties of Human Insulin Amyloid Spherulites. *Journal of Physical Chemistry B.* 2018;122(12):3101-3112. doi:10.1021/ACS.JPCB.8B01779
27. Santangelo MG, Foderà V, Militello V, Vetri V. Back to the oligomeric state: PH-induced dissolution of concanavalin A amyloid-like fibrils into non-native oligomers. *RSC Adv.* 2016;6(79):75082-75091. doi:10.1039/C6RA16690C
28. Anselmo S, Sancataldo G, Foderà V, Vetri V. α -casein micelles-membranes interaction: Flower-like lipid protein coaggregates formation. *Biochimica et Biophysica Acta (BBA) - General Subjects.* 2022;1866(10):130196. doi:10.1016/J.BBAGEN.2022.130196
29. Fennema Galparsoro D, Zhou X, Jaaloul A, Piccirilli F, Vetri V, Foderà V. Conformational Transitions upon Maturation Rule Surface and pH-Responsiveness of α -Lactalbumin Microparticulates. *ACS Appl Bio Mater.* 2021;4(2):1876-1887. doi:10.1021/ACSABM.0C01541
30. Bolisetty S, Reinhold N, Zeder C, Orozco MN, Mezzenga R. Efficient purification of arsenic-contaminated water using amyloid-carbon hybrid membranes. *Chemical Communications.* 2017;53(42):5714-5717. doi:10.1039/C7CC00406K
31. Zhang Q, Bolisetty S, Cao Y, et al. Selective and Efficient Removal of Fluoride from Water: In Situ Engineered Amyloid Fibril/ZrO₂ Hybrid Membranes. *Angewandte Chemie - International Edition.* 2019;58(18):6012-6016. doi:10.1002/ANIE.201901596
32. Peydayesh M, Suter MK, Bolisetty S, et al. Amyloid Fibrils Aerogel for Sustainable Removal of Organic Contaminants from Water. *Advanced Materials.* 2020;32(12). doi:10.1002/ADMA.201907932
33. Singh P, Kumar R, Sabapathy SN, Bawa AS. Functional and Edible Uses of Soy Protein Products. *Compr Rev Food Sci Food Saf.* 2008;7(1):14-28. doi:10.1111/J.1541-4337.2007.00025.X

34. Song F, Tang DL, Wang XL, Wang YZ. Biodegradable soy protein isolate-based materials: A review. *Biomacromolecules*. 2011;12(10):3369-3380. doi:10.1021/BM200904X/ASSET/IMAGES/MEDIUM/BM-2011-00904X_0008.GIF
35. Stie MB, Kalouta K, da Cunha CFB, Feroze HM, Vetri V, Foderà V. Sustainable strategies for waterborne electrospinning of biocompatible nanofibers based on soy protein isolate. *Sustainable Materials and Technologies*. 2022;34:e00519. doi:10.1016/J.SUSMAT.2022.E00519
36. Fukushima D. Soy proteins. *Handbook of Food Proteins*. Published online January 1, 2011:210-232. doi:10.1533/9780857093639.210
37. Jaramillo DP, Roberts RF, Coupland JN. Effect of pH on the properties of soy protein-pectin complexes. *Food Research International*. 2011;44(4):911-916. doi:10.1016/J.FOODRES.2011.01.057
38. Álvarez-Castillo E, Aguilar JM, Bengoechea C, López-Castejón ML, Guerrero A. Rheology and Water Absorption Properties of Alginate-Soy Protein Composites. *Polymers* 2021, Vol 13, Page 1807. 2021;13(11):1807. doi:10.3390/POLYM13111807
39. Liu J, Su D, Yao J, Huang Y, Shao Z, Chen X. Soy protein-based polyethylenimine hydrogel and its high selectivity for copper ion removal in wastewater treatment. *J Mater Chem A Mater*. 2017;5(8):4163-4171. doi:10.1039/C6TA10814H
40. Vetri V, Foderà V. The route to protein aggregate superstructures: Particulates and amyloid-like spherulites. *FEBS Lett*. 2015;589(19):2448-2463. doi:10.1016/J.FEBSLET.2015.07.006
41. Stringari C, Cinquin A, Cinquin O, Digman MA, Donovan PJ, Gratton E. Phasor approach to fluorescence lifetime microscopy distinguishes different metabolic states of germ cells in a live tissue. *Proc Natl Acad Sci U S A*. 2011;108(33):13582-13587. doi:10.1073/PNAS.1108161108
42. Data Tables | Fluorescence Lifetime Standards | ISS. Accessed August 2, 2022. https://iss.com/resources/reference/data_tables/FL_LifetimeStandards.html
43. Fluorescence quantum yields (QY) and lifetimes (τ) for Alexa Fluor dyes—Table 1.5 | Thermo Fisher Scientific - IT. Accessed August 2, 2022. <https://www.thermofisher.com/it/en/home/references/molecular-probes-the-handbook/tables/fluorescence-quantum-yields-and-lifetimes-for-alexa-fluor-dyes.html>
44. Lagergren, S., About the Theory of so Called Adsorption of Soluble Substances, *Kungliga Svenska Vetenskapsakademiens Handlingar*, 24, 1-39, 1898. Accessed August 2, 2022. <http://www.sciepub.com/reference/163936>
45. Removal of Heavy Metals from Mine Waters by Natural Zeolites. Published online 2005. doi:10.1021/es048482s
46. Tan KL, Hameed BH. Insight into the adsorption kinetics models for the removal of contaminants from aqueous solutions. *J Taiwan Inst Chem Eng*. 2017;74:25-48. doi:10.1016/J.JTICE.2017.01.024
47. Freundlich H. Über die Adsorption in Lösungen. *Zeitschrift für Physikalische Chemie*. 1907;57U(1):385-470. doi:10.1515/ZPCH-1907-5723/HTML
48. Langmuir I. The adsorption of gases on plane surfaces of glass, mica and platinum. *J Am Chem Soc*. 1918;40(9):1361-1403. doi:10.1021/JA02242A004
49. Zölls S, Gregoritz M, Tantipolphan R, et al. How subvisible particles become invisible—relevance of the refractive index for protein particle analysis. *J Pharm Sci*. 2013;102(5):1434-1446. doi:10.1002/jps.23479
50. Piccirilli F, Schirò G, Vetri V, Lupi S, Perucchi A, Militello V. Decoding vibrational states of Concanavalin A amyloid fibrils. *Biophys Chem*. 2015;199:17-24. doi:10.1016/J.BPC.2015.02.007
51. Fabian H, Mentele W. Infrared Spectroscopy of Proteins. *Handbook of Vibrational Spectroscopy*. Published online August 15, 2006. doi:10.1002/0470027320.S8201

52. Usoltsev D, Sitnikova V, Kajava A, Uspenskaya M. Systematic FTIR Spectroscopy Study of the Secondary Structure Changes in Human Serum Albumin under Various Denaturation Conditions. *Biomolecules*. 2019;9(8). doi:10.3390/BIOM9080359
53. Jackson M, Mantsch HH. Protein secondary structure from FT-IR spectroscopy: correlation with dihedral angles from three-dimensional Ramachandran plots. <https://doi.org/10.1139/v91-240>. 2011;69(11):1639-1642. doi:10.1139/V91-240
54. Wang C, Jiang L, Wei D, et al. Effect of Secondary Structure determined by FTIR Spectra on Surface Hydrophobicity of Soybean Protein Isolate. *Procedia Eng*. 2011;15:4819-4827. doi:10.1016/J.PROENG.2011.08.900
55. Peydayesh M, Bolisetty S, Mohammadi T, Mezzenga R. Assessing the Binding Performance of Amyloid-Carbon Membranes toward Heavy Metal Ions. *Langmuir*. 2019;35(11):4161-4170. doi:10.1021/ACS.LANGMUIR.8B04234
56. Foderà V, Groenning M, Vetri V, et al. Thioflavin T hydroxylation at basic pH and its effect on amyloid fibril detection. *Journal of Physical Chemistry B*. 2008;112(47):15174-15181. doi:10.1021/JP805560C/SUPPL_FILE/JP805560C_SI_001.PDF
57. di Carlo MG, Minicozzi V, Foderà V, et al. Thioflavin T templates amyloid β (1–40) conformation and aggregation pathway. *Biophys Chem*. 2015;206:1-11. doi:10.1016/J.BPC.2015.06.006
58. Lindberg DJ, Wranne MS, Gilbert Gatty M, Westerlund F, Esbjörner EK. Steady-state and time-resolved Thioflavin-T fluorescence can report on morphological differences in amyloid fibrils formed by A β (1–40) and A β (1–42). *Biochem Biophys Res Commun*. 2015;458(2):418-423. doi:10.1016/J.BBRC.2015.01.132
59. de Luca G, Fennema Galparsoro D, Sancataldo G, Leone M, Foderà V, Vetri V. Probing ensemble polymorphism and single aggregate structural heterogeneity in insulin amyloid self-assembly. *J Colloid Interface Sci*. 2020;574:229-240. doi:10.1016/J.JCIS.2020.03.107
60. Morando MA, Venturella F, Sollazzo M, et al. Solution structure of recombinant Pvfp-5 β reveals insights into mussel adhesion. *Communications Biology* 2022 5:1. 2022;5(1):1-10. doi:10.1038/s42003-022-03699-w
61. Sackett DL, Wolff J. Nile red as a polarity-sensitive fluorescent probe of hydrophobic protein surfaces. *Anal Biochem*. 1987;167(2):228-234. doi:10.1016/0003-2697(87)90157-6
62. Levitt JA, Chung PH, Suhling K. Spectrally resolved fluorescence lifetime imaging of Nile red for measurements of intracellular polarity. *J Biomed Opt*. 2015;20(9):096002. doi:10.1117/1.JBO.20.9.096002
63. Barber-Zucker S, Shaanan B, Zarivach R. Transition metal binding selectivity in proteins and its correlation with the phylogenomic classification of the cation diffusion facilitator protein family. *Scientific Reports* 2017 7:1. 2017;7(1):1-12. doi:10.1038/s41598-017-16777-5
64. Cox JD, Hunt JA, Compher KM, Fierke CA, Christianson DW. Structural influence of hydrophobic core residues on metal binding and specificity in carbonic anhydrase II. *Biochemistry*. 2000;39(45):13687-13694. doi:10.1021/BI001649J
65. Chen Q yu, Yang L, Liu L, et al. Combined forms of Pb and its detoxification and absorption in *Cladophora rupestris* subcells. *Spectrochim Acta A Mol Biomol Spectrosc*. 2021;248:119190. doi:10.1016/J.SAA.2020.119190
66. Guibaud G, Tixier N, Bouju A, Baudu M. Relation between extracellular polymers' composition and its ability to complex Cd, Cu and Pb. *Chemosphere*. 2003;52(10):1701-1710. doi:10.1016/S0045-6535(03)00355-2

67. Huamani-Palomino RG, Jacinto CR, Alarcón H, et al. Chemical modification of alginate with cysteine and its application for the removal of Pb(II) from aqueous solutions. *Int J Biol Macromol*. 2019;129:1056-1068. doi:10.1016/J.IJBIOMAC.2018.09.096
68. Cazalbou S, Bertrand G, Drouet C. Tetracycline-loaded biomimetic apatite: An adsorption study. *Journal of Physical Chemistry B*. 2015;119(7):3014-3024. doi:10.1021/JP5116756
69. Ouyang D, Zhuo Y, Hu L, Zeng Q, Hu Y, He Z. Research on the Adsorption Behavior of Heavy Metal Ions by Porous Material Prepared with Silicate Tailings. *Minerals* 2019, Vol 9, Page 291. 2019;9(5):291. doi:10.3390/MIN9050291
70. Cataldo S, lo Meo P, Conte P, di Vincenzo A, Milea D, Pettignano A. Evaluation of adsorption ability of cyclodextrin-calixarene nanosponges towards Pb²⁺ ion in aqueous solution. *Carbohydr Polym*. 2021;267. doi:10.1016/J.CARBPOL.2021.118151
71. Zhang Z, He S, Zhang Y, et al. Spectroscopic investigation of Cu²⁺, Pb²⁺ and Cd²⁺ adsorption behaviors by chitosan-coated argillaceous limestone: Competition and mechanisms. *Environmental Pollution*. 2019;254. doi:10.1016/J.ENVPOL.2019.07.106
72. Liu L, Huang Y, Meng Y, et al. Investigating the adsorption behavior and quantitative contribution of Pb²⁺ adsorption mechanisms on biochars by different feedstocks from a fluidized bed pyrolysis system. *Environ Res*. 2020;187:109609. doi:10.1016/J.ENVRES.2020.109609
73. He S, Li Y, Weng L, et al. Competitive adsorption of Cd²⁺, Pb²⁺ and Ni²⁺ onto Fe³⁺-modified argillaceous limestone: Influence of pH, ionic strength and natural organic matters. *Sci Total Environ*. 2018;637-638:69-78. doi:10.1016/J.SCITOTENV.2018.04.300
74. Santangelo MG, Foderà V, Militello V, Vetri V. Back to the oligomeric state: pH-induced dissolution of concanavalin A amyloid-like fibrils into non-native oligomers. *RSC Adv*. 2016;6(79):75082-75091. doi:10.1039/C6RA16690C
75. Zhou X, Fennema Galparsoro D, Østergaard Madsen A, et al. Polysorbate 80 controls Morphology, structure and stability of human insulin Amyloid-Like spherulites. *J Colloid Interface Sci*. 2022;606:1928-1939. doi:10.1016/J.JCIS.2021.09.132
76. C. F. Baes and R. S. Mesmer: The Hydrolysis of Cations. John Wiley & Sons, New York, London, Sydney, Toronto 1976. 489 Seiten, Preis: £ 18.60. *Berichte der Bunsengesellschaft für physikalische Chemie*. 1977;81(2):245-246. doi:10.1002/BBPC.19770810252
77. Cataldo S, Lando G, Milea D, Orecchio S, Pettignano A, Sammartano S. A novel thermodynamic approach for the complexation study of toxic metal cations by landfill leachate.
78. Liu J, Su D, Yao J, Huang Y, Shao Z, Chen X. Soy protein-based polyethylenimine hydrogel and its high selectivity for copper ion removal in wastewater treatment. *J Mater Chem A Mater*. 2017;5(8):4163-4171. doi:10.1039/C6TA10814H
79. Soon WL, Peydayesh M, Mezzenga R, Miserez A. Plant-based amyloids from food waste for removal of heavy metals from contaminated water. *Chemical Engineering Journal*. 2022;445:136513. doi:10.1016/J.CEJ.2022.136513
80. Yang F, Yang Q, Chen M, Luo C, Chen W, Yang P. Toxic metal ion sequestration by amyloid-mediated fast coacervation. *Cell Rep Phys Sci*. 2021;2(3):100379. doi:10.1016/J.XCRP.2021.100379
81. Soon WL, Peydayesh M, Mezzenga R, Miserez A. Plant-based amyloids from food waste for removal of heavy metals from contaminated water. *Chemical Engineering Journal*. 2022;445:136513. doi:10.1016/J.CEJ.2022.136513